IOP PUBLISHING PHYSICS IN MEDICINE AND BIOLOGY

Phys. Med. Biol. **53** (2008) 1099–1113 doi:10.1088/0031-9155/53/4/019

Development of a simplified simulation model for performance characterization of a pixellated CdZnTe multimodality imaging system

P Guerra[1], **A Santos**[1] **and D G Darambara**[2]

[1] Departamento de Ingeniería Electrónica, Universidad Politécnica de Madrid, Ciudad Universitaria s/n, 28040 Madrid, Spain
[2] Joint Department of Physics, Royal Marsden NHS Foundation Trust and The Institute of Cancer Research, Fulham Road, London SW3 6JJ, UK

E-mail: pguerra@die.um.es

Received 13 September 2007, in final form 15 January 2008
Published 1 February 2008
Online at stacks.iop.org/PMB/53/1099

Abstract

Current requirements of molecular imaging lead to the complete integration of complementary modalities in a single hybrid imaging system to correlate function and structure. Among the various existing detector technologies, which can be implemented to integrate nuclear modalities (PET and/or single-photon emission computed tomography with x-rays (CT) and most probably with MR, pixellated wide bandgap room temperature semiconductor detectors, such as CdZnTe and/or CdTe, are promising candidates. This paper deals with the development of a simplified simulation model for pixellated semiconductor radiation detectors, as a first step towards the performance characterization of a multimodality imaging system based on CdZnTe. In particular, this work presents a simple computational model, based on a 1D approximate solution of the Schockley–Ramo theorem, and its integration into the Geant4 application for tomographic emission (GATE) platform in order to perform accurately and, therefore, improve the simulations of pixellated detectors in different configurations with a simultaneous cathode and anode pixel readout. The model presented here is successfully validated against an existing detailed finite element simulator, the multi-geometry simulation code, with respect to the charge induced at the anode, taking into consideration interpixel charge sharing and crosstalk, and to the detector charge induction efficiency. As a final point, the model provides estimated energy spectra and time resolution for ^{57}Co and ^{18}F sources obtained with the GATE code after the incorporation of the proposed model.

(Some figures in this article are in colour only in the electronic version)

1. Introduction

In general, the field of non-invasive multimodality imaging involves the incorporation of two or more medical imaging modalities, usually within the setting of a single examination, to answer the question of interest. For example, the use of dual- or triple-labelled optical or nuclear medicine 'reporter' agents, the performance of ultrasound or optical studies within the MR and the combination of single-photon emission computed tomography (SPECT) with x-ray computed tomography (CT) (Moseley and Donnan 2004, Cherry 2006) are some of the imaging modalities. The goal of any multimodal imaging approach is to provide information on the exact localization, the extent and metabolic activity of the target tissue and its function or interaction and any functional changes within the surrounding tissues. These requirements lead towards hybrid systems where imaging modalities are truly integrated into a single device, using simultaneous rather than sequential scanning, and therefore the resulting multidimensional images are time and space accurately aligned by their formation.

Among the various detector technologies currently available for integrating multiple imaging modalities, such as nuclear modalities (PET and/or SPECT) with x-rays (CT) and/or MR (Wagenaar *et al* 2007), in a single hybrid system, pixellated wide bandgap room temperature semiconductor detectors, such as CdZnTe and/or CdTe, are promising candidates due to their high inherent spatial resolution and high energy resolution within a wide range of energies that allows better scatter rejection and multi-isotope acquisition (Darambara 2006). Moreover the interest on semiconductor materials for gamma-ray imaging has been steadily increased in the last decade, supported by recent significant advances in crystal growth and electrode geometries (Szeles and Eissler 1998, Funaki *et al* 1999, Szeles 2004, Seifert *et al* 2005).

Hitherto a few authors (Visvikis *et al* 2005, Habte *et al* 2007) have studied the full potential of a CdZnTe-based PET scanner, with results that can be questioned due to an incomplete modelling of the material in the simulation code implemented. In particular, the strong dependence of induced signals on the pixel-to-thickness ratio, the electrical field and the depth of interaction requires special consideration, or otherwise simulation results can lead to an over- or under-estimation of system sensitivity.

Such performance analyses are based on simulation tools that include detailed models of the underlying physics and scanner characteristics. Among these tools, the Geant4 application for tomographic emission (GATE) (Jan *et al* 2004) has recently become very popular due to its flexibility in modelling various existing scanners (Jan *et al* 2005, 2004, Lamare *et al* 2004, Schmidtlein *et al* 2004, 2006) and the accuracy of its simulations in predicting experimental measurements. Nevertheless, existing GATE models focus mostly on scintillator-based detectors, and the accurate modelling of the CdZnTe properties and characteristics is rather limited.

A number of publications (Hamel and Paquet 1996, Glière *et al* 2000, Heanue *et al* 1997, Mathy *et al* 2004) have in the past dealt with the modelling of charge transport in semiconductor detectors. Early works assumed a uniform electric field, while later works tended to consider more complicated electric field profiles, where numerical techniques become inevitable. For example, the 3D model presented by Mathy *et al* (2004) involves finite element transient computation of the adjoint transport equation, a Monte Carlo simulation of the photon transport and signal processing carried out by the electronics, including an accurate noise model (Picone *et al* 2003).

The aim of this work is to present a simple computational model of pixellated CdZnTe detectors and to integrate it into the GATE code in order to improve simulations of pixellated detectors in different configurations with simultaneous cathode and anode pixel readout. This

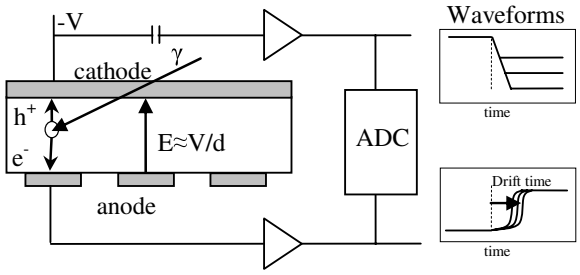

Figure 1. Basic diagram of a pixellated CdZnTe detector with biasing voltage V and thickness d. The waveforms of the signals expected at the anode and cathode are shown on the right.

model, based on a 1D approximate solution of the Schockley–Ramo theorem, will be compared with detailed finite element simulations of the electron–hole movements within the material. After that, GATE simulation plots will be provided for a 5 mm thick CdZnTe detector. Finally, the benefits of the proposed approach will be discussed.

2. Material and methods

2.1. Detector model

The proposed multimodality scanner consists of several detector modules, each one comprising one or more CdZnTe slabs. The interaction of a gamma ray with the semiconductor material causes the excited electrons to jump to higher energy bands, creating an excess of mobile charge carriers; under the presence of an electric field both electrons and holes drift towards the anode and the cathode electrodes respectively, inducing a voltage signal that provides information about the deposited energy and the position of interaction, as shown in figure 1. These charge carriers also undergo diffusion and recombination as well as trapping and detrapping to defect states. Trapping and detrapping are by far the most detrimental effects on the energy resolution of wide bandgap semiconductor detectors (Hamel and Paquet 1996).

Unlike a scintillator crystal, in a semiconductor detector there is a significant dependence of the induced charge on the interaction point within the slab. Single polarity charge sensing through a coplanar grid anode has been widely applied to overcome the poor hole transport; however, cathode sensing is usually required to resolve the depth of interaction and the timing of the event. In such a detector configuration, the induced signal on the anode is almost independent of the depth of interaction while the cathode signal varies approximately linearly with the distance to the cathode. These and other effects are very well explained by the Schockley–Ramo theorem (Ramo 1939).

The standard model for charge collection in semiconductors is based on the continuity equation for an excess charge carrier's densities. The charge induced at a selected electrode k by the drift of the electron density $n(\mathbf{x}, \mathbf{t})$, during the time interval t', is calculated using Ramo's theorem as (Mathy *et al* 2004)

$$\Delta Q_k = \int_0^{t'} \mathrm{d}t \int_\Omega n(\mathbf{x}, t) \cdot \mu_\mathrm{e} \cdot \nabla\psi(\mathbf{x}) \cdot \nabla\varphi_k(\mathbf{x})\, \mathrm{d}\Omega, \tag{1}$$

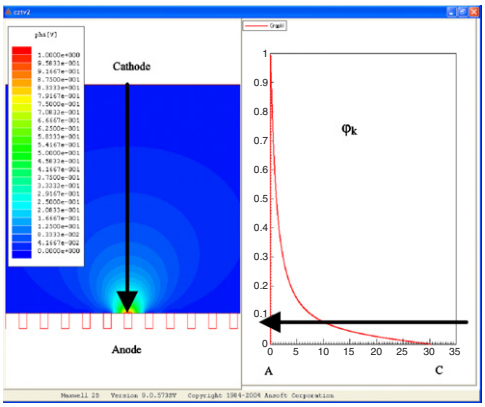

Figure 2. FEM simulation for the computation of ϕ_0 with a 32 mm thick CdZnTe slab on the left and weighting function along the line between the anode A and the cathode C on the right.

where $\psi(\mathbf{x})$ is the operating potential, $\varphi(\mathbf{x})$ is the weighting potential and μ_e is the electron mobility. In order to be able to incorporate Ramo's theorem into the GATE code at a reasonable computational cost, several simplifications are required.

2.1.1. Simple model. A feasible solution can be attained by assuming a 1D version of Ramo's theorem (He 2001) and combining it with charge loss by trapping or recombination; trapping is the most dominant process in CdZnTe. In this case, the charge ΔQ_k induced at anode k by a gamma-ray deposition at x_o that creates N_o electrons with mobility μ_e and lifetime τ_e travelling along the path L towards the anode is approximately calculated by

$$\begin{aligned} \Delta Q_k &= q \cdot N_0 \cdot \int_L \mathrm{e}^{-(x-x_0)/\lambda_e} \cdot \varphi_k'(x) \cdot \mathrm{d}x \\ \lambda_e &= (\mu_e \cdot \tau_e) \cdot E = (\mu_e \cdot \tau_e) \cdot V/d, \end{aligned} \tag{2}$$

where q is the electron charge, V is the biasing voltage, d is the detector thickness and E is the electric field, which is assumed to be uniform.

The value of the weighting potential φ_k is mainly a function of the material properties and the detector geometry, and can be computed in detail using the finite element method (FEM), as shown in figure 2. As an example, if a semiconductor detector consists of two parallel readout plates, one at the anode and the other at the cathode, the weighting potential can be approximated by $\varphi_k(x) = x/d$ and the Hetch equation for the electrons can be derived from equation (1):

$$\Delta Q_k = N_0 \cdot \frac{\lambda_e \cdot q}{d} \cdot \left(1 - \exp\left(-\frac{d - x_0}{\lambda_e}\right)\right). \tag{3}$$

In order to efficiently compute the induced charge ΔQ_k for a given energy deposition $N_o q$ at a location x_o, an analytical form of equation (1) is favoured. Although analytical solutions of the charge transport in a semiconductor detector (Barrett *et al* 1995, Hamel and Paquet 1996) usually calculate the weighting function $\varphi_k(x)$ as an infinite sum of terms, they are still time consuming and computationally costly, and therefore further simplification is required. The simplest approximation is to assume that the weighting function has an exponential decay τ_a while the boundary conditions at the anode and the cathode are satisfied, as is shown in

equation (4). The decay constant τ_a incorporates geometric dependences and is derived as the value that provides the best fit between the simplified equation and the actual 3D model (Castoldi *et al* 1996):

$$\begin{aligned}
\varphi_k(x) &\approx \frac{e^{-d/\tau_a}}{1-e^{-d/\tau_a}} \cdot (e^{x/\tau_a} - 1) \\
\varphi_k'(x) &\approx \frac{e^{-d/\tau_a}}{1-e^{-d/\tau_a}} \cdot \frac{1}{\tau_a} \cdot e^{x/\tau_a} \\
\varphi_k(0) &= 0 \qquad \varphi(d) = 1.
\end{aligned} \tag{4}$$

Assuming this approximation, it is shown that the induced charge ΔQ_k at the anode is given by the following expression:

$$\begin{aligned}
\Delta Q_k &= \frac{\lambda_e^* \cdot N_0 \cdot q}{\tau_a} \cdot \frac{\exp\left(\frac{x_0-d}{\lambda_e}\right)}{1-\exp\left(-\frac{d}{\tau_a}\right)} \cdot \left(1 - \exp\left(\frac{x_0-d}{\lambda_e^*}\right)\right) \\
\lambda_e^* &= \frac{\lambda_e \cdot \tau_a}{\lambda_e - \tau_a}.
\end{aligned} \tag{5}$$

The detector charge induction efficiency (CIE) is computed as the ratio of the readout energy to the deposited energy, and it is a function of depth x, material thickness d, material properties λ_e and indirectly of the geometry through τ_a:

$$\mathrm{CIE} = \frac{\lambda_e^*}{\tau_a} \cdot \frac{\exp\left(\frac{x_0-d}{\lambda_e}\right)}{1-\exp\left(-\frac{d}{\tau_a}\right)} \cdot \left(1 - \exp\left(\frac{x_0-d}{\lambda_e^*}\right)\right). \tag{6}$$

2.1.2. Charge sharing model. The simplified model shown in equation (5) is extended to take into account interpixel charge sharing and crosstalk. In order to estimate the shared charge, we will assume that the energy deposition at x_o generates an electron cloud of a finite size which, as a first approximation and for the benefit of the computational efficiency, is modelled as a cube of side D, although other models, such as a sphere, could be also considered. The simulation model implemented computes the proportion of the cube that is confined within each pixel and creates a new GATE pulse at each of the detector pixels involved. Charge sharing will be mostly observed in areas near the edges, where a fraction of this charge will belong to one pixel and another fraction to a neighbouring pixel, as is shown in figure 3.

2.1.3. Crosstalk model. Crosstalk refers to charge induction at anode j caused by charges that are collected by anode i, as is shown in figure 4. According to Ramo's theorem, crosstalk is explained by a weighting function whose volume of sensitivity extends beyond the limits of the pixel volume, a situation that is shown in figure 4, and can be approximated as

$$\Delta Q_j = -N_0 \cdot q \cdot \varphi_j(r_j). \tag{7}$$

According to equation (7), the explicit value of the weighting potential is required, which in the model implemented here is estimated based on a 3D analytical solution of the Laplace equation as described in Castoldi *et al* (1996). This solution assumes that the 3D volume is contained between two infinite parallel planes representing the surfaces of the detector, and the equations provided satisfy the original Dirichlet conditions of the two planes. Under the assumptions considered, the exact solution of the Laplace equation can be expressed as a series of elementary functions φ_0 due to the reflected dipole layers equally spaced at $2kd$:

$$\varphi_j(r_j) = \sum_{k=-\infty}^{k=\infty} \varphi_0(x, y, z - 2kd). \tag{8}$$

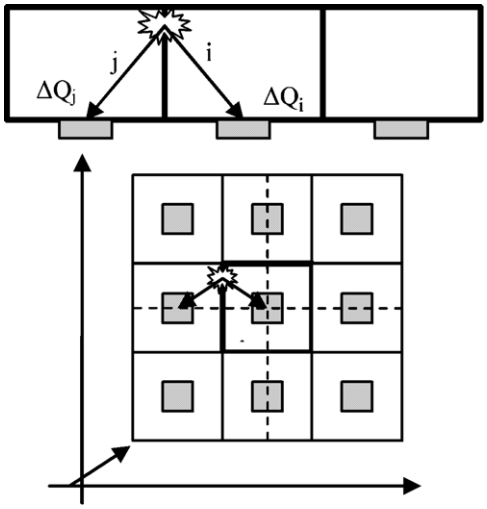

Figure 3. Charge sharing diagram. A cloud of electrons is generated, which may drift to different pixels.

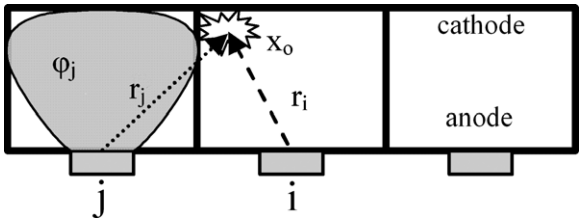

Figure 4. Crosstalk diagram. The pixel weighting potential extends beyond the pixel limits inducing crosstalk.

In the particular case where the pad is considered as rectangular, the solution reduces to

$$\varphi_0(x, y, z) = \frac{1}{2\pi} \cdot \left(\begin{array}{l} \arctan \frac{(a-\xi)(b-\eta)}{z\sqrt{(a-\xi)^2+(b-\eta)^2+z^2}} + \arctan \frac{(a-\xi)\eta}{z\sqrt{(a-\xi)^2+\eta^2+z^2}} + \cdots \\ \arctan \frac{\xi(b-\eta)}{z\sqrt{\xi^2+(b-\eta)^2+z^2}} + \arctan \frac{\xi\eta}{z\sqrt{\xi^2+\eta^2+z^2}} \end{array} \right)$$
$$\xi = \frac{(x - x_1)(x_2 - x_1) + (y - y_1)(y_2 - y_1)}{a} \tag{9}$$
$$\eta = \frac{-(x - x_1)(y_2 - y_1) + (y - y_1)(x_2 - x_1)}{b},$$

where a and b are the readout pad's length and width respectively, (x_1, y_1) (x_2, y_2) (x_3, y_3) (x_4, y_4) are the j pad's corner coordinates and (x, y, z) is the interaction point x_o with respect to the anode j.

2.1.4. Timing model. Finally, in PET imaging an accurate timing of the event is required. However, the long charge collection time of charge carriers within the semiconductor material limits to some degree the excellent spectroscopic characteristics of the pixellated CdZnTe detectors resulting in their poor performance with respect to timing resolution. The model

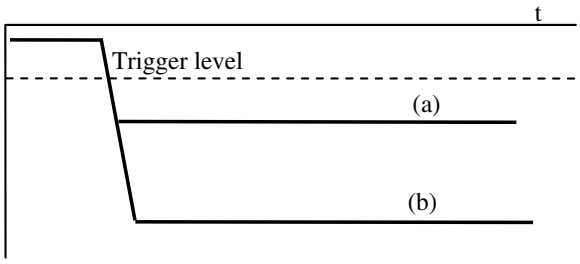

Figure 5. Cathode waveform representation of two simultaneous depositions with the same energy but at different points within the crystal: (a) near the anode and (b) near the cathode.

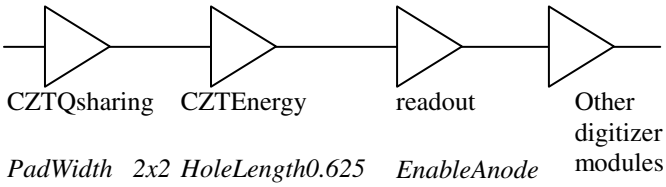

Figure 6. GATE digitizer setup after its extension to include CdZnTe modelling.

implemented considers a cathode-based timing, where the timestamp is regarded as the time point where the energy induced at the cathode crosses a certain threshold E_{trig} value above the noise level. Under these considerations, the direct application of Ramo's theorem leads to the following estimation of the timewalk Δt:

$$\Delta t = -\frac{\tau_c}{v_e}\ln\left(-\frac{E_{\text{trig}}}{E_o}\frac{1-\exp\left(-\frac{d}{\tau_c}\right)}{\exp\left(-\frac{x_0}{\tau_c}\right)}+1\right), \tag{10}$$

where x_0 is the interaction position, E_o is the deposited energy, v_e is the electron drift velocity, E_{trig} is the triggering level, τ_c is the fitting parameter with respect to the cathode weighting potential and d is the material thickness.

Figure 5 illustrates, as an example, the expected pulse shape of two simultaneous and of equal energy depositions at two different points within the detector. As the figure shows, the signal amplitude of depositions close to the anode may not be high enough to provide a reasonable timestamp. Moreover, the leading edge slope depends on the deposited energy, introducing an additional timewalk.

2.2. GATE extensions

GATE v3.0.0 has been extended to include the models previously presented as optional digitizer modules. The original source code is extremely well structured and documented making it feasible to introduce such custom modifications.

In the first place, the *GatePulse* class has been extended in order to enable tracking of the readout energies at the anode and the cathode. Next, as is shown in the diagram of figure 6, a new digitizer module called *CZTQsharing* models the collection of the electrons by different pixels by distributing the generated charge after the gamma-ray–matter interaction into the original pixel and its neighbours, as described in section 2.1.2. Additionally, the digitizer module called *CZTEnergy* estimates the charge induced at every pixel k, as the combination

Table 1. CdZnTe main physical properties.

Density (g cm^{-3})	5.78	Dielectric constant	10.9
Resistivity (cm)	3×10^{10}	Pair creation energy (eV)	4.64
Electron lifetime (s)	3×10^{-6}	Electron mobility (cm^2 (V s)$^{-1}$)	1000
Hole lifetime (s)	10^{-6}	Hole mobility (cm^2 (V s)$^{-1}$)	50–80

of the charge induced by moving electrons and holes within the pixel as given by equation (5) and the crosstalk produced by moving charges at neighbouring pixels as expressed by equation (7).

Finally different modules, including *GateReadout* and *GateBlurring*, have been modified in order to account for the fact that two energies, anode and cathode, are being read out.

3. Results

3.1. Model validation

In order to validate this simplified model, the multi-geometry simulation code (MGS) (Medina *et al* 2004) has been employed. This code, which runs under Matlab v7.1 (MathWorks Inc., Natick, MA, USA), is a 3D FEM simulator that was originally developed to characterize germanium detectors, although, in fact, it places no restriction on the actual geometry or material under consideration, and therefore it may also be used to simulate generic CdZnTe detectors (Dirks *et al* 2004). The FEM engine consists of six steps, as follows.

- Geometry definition.
- Calculation of the electric field starting from the solution of the Poisson equation.
- Implementation of charge carrier transport in a semi-conducting medium.
- Computation of trajectories of charge carriers for arbitrary interaction points.
- Weighting potential and weighting field resolution.
- Application of the Ramo theorem, which provides the resulting charge recovery at the readout contacts.

The Poisson equation was solved after 100 loops of the Gauss–Seidel-based successive over relaxation (SOR) method for a 5×5 pixel planar detector with a pixel size of $2 \times 2 \times 5$ mm^3, out of which only the centre of the pixel is considered; this setup is meant to avoid the influence of the lateral boundary conditions on the pixel under simulation.

With the aid of some Matlab ad hoc scripts, the simulator is capable of taking the hit root files generated by GATE as input, computing the charge induced at the anodes and the cathode as well as estimating the waveforms at each electrode. Subsequently, hits are transformed into singles and the detector energy spectrum is computed.

The material physical properties, summarized in table 1, are taken from the specifications provided by eV Products (eV PRODUCTS, Saxonburg, PA, USA) for $Cd_{0.9}Zn_{0.1}Te$.

The model-based CIE, as given by equation (6), at the centre of a $2 \times 2 \times 5$ mm^3 CdZnTe pixel has been computed for different bias voltages and electron mobilities and, as shown in figure 7, the profile very well agrees with the simulated solution of the drift-diffusion equation provided by the MGS. The model parameter τ_a is computed as the value that provides the best fit between equation (9) and the proposed simplified $\phi(x)$ of equation (4).

Figure 8 shows the difference in percentage between the MGS simulation and the model described. The average error between the estimated CIE provided by the simplified model

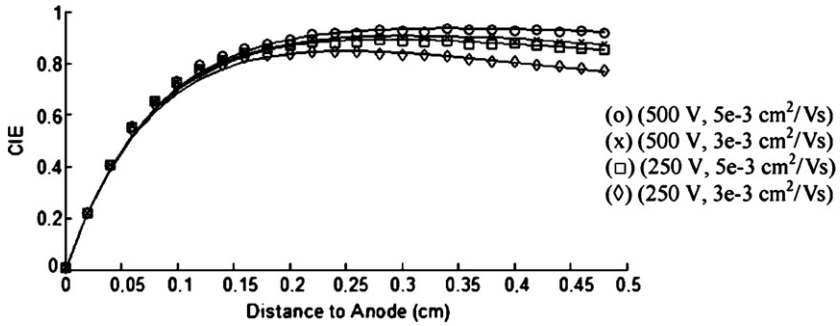

Figure 7. MGS simulated (symbol) and model estimated (solid line) CIE at the pixel centre for a 5 mm thick CdZnTe detector for different combinations of bias and electron mobilities.

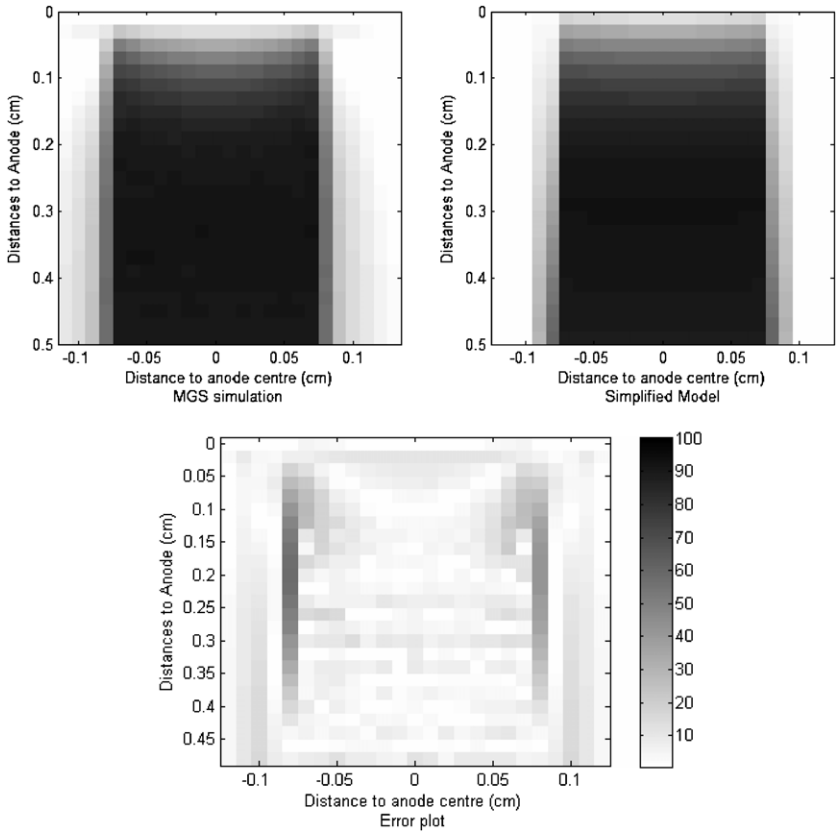

Figure 8. MGS simulated (top left) and simplified model (top right) CIE for a 2 × 2 × 5 mm^3 pixel at 500 V bias with $\mu\tau_e = 3 \times 10^{-3}$ cm^2 V^{-1} and without noise. The difference (in percent) of error between both models is also shown (bottom).

and the FEM simulation is lower than 5% and the maximum discrepancies between the two models take place around the pixel 'virtual' edges.

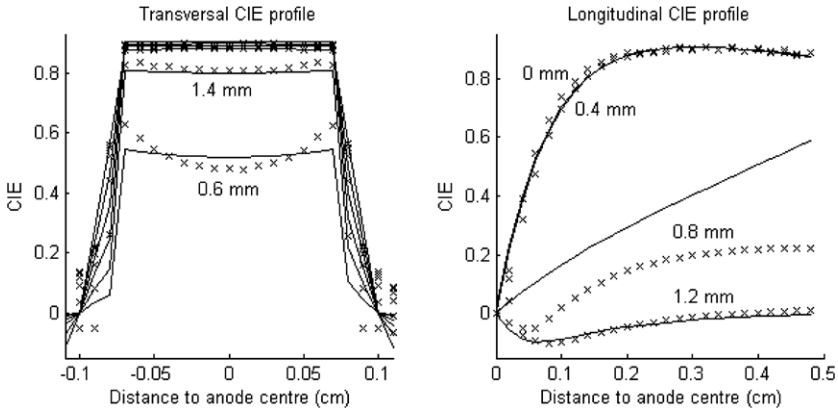

Figure 9. On the left, the simplified model (solid line) versus MGS simulated (x) pixel CIE for a $2 \times 2 \times 5$ mm^3 pixel at 500 V bias with $\mu\tau_e = 3 \times 10^{-3}$ cm^2 V^{-1} and without noise for several segments along the pixel at 0.6 mm, 1.4 mm, 2.2 mm, 3.0 mm, 3.8 mm and 4.6 mm to the anode. On the right, the simplified model (solid line) versus MGS simulated (x) pixel CIE at 0 mm, 0.4 mm, 0.8 mm and 1.2 mm to the anode centre.

Figures 8 and 9 show the estimated 2D CIE when all the effects are included and where the first 21 terms of the elementary function φ_0 were used for the crosstalk estimation. Both efficiency maps of figure 8 demonstrate that the proposed model reasonably approximates the numerical computations but at a much lower computational cost. On the other hand, the longitudinal profiles of figure 9 show a clear mismatch between the simple model and the FEM simulation at 0.8 mm from the anode centre, which corresponds to the pixel edge. This discrepancy is explained by the fact that at the pixel edges the electric field lines bend and therefore the uniform field assumption is no longer valid; moreover close to the anode, the charge carriers follow a path very different to that applied in the model. It may also be argued that at the pixel edge the weighting function and, correspondingly, the CIE drop sharply and any minor mismatch between models yields a very high relative error.

For the simulations presented in this work, tracking electrons and holes in the MGS took around 26 s per gamma-ray interaction while the model provided an estimate at a negligible computational cost.

In CdTe and CdZnTe detectors, the timing resolution is determined mostly by the pulse shape, which consists of a mixture of electrons and holes. Therefore, it is important to study how the slow holes contribute to the signal, when fast shaping is applied in order to minimise the contribution of the holes. In this scenario, timing resolution is determined mainly by event-by-event variation of the electron rise time and by electronic noise.

In order to validate the timing model of equation (10), 500 singles were generated for a $2 \times 2 \times 5$ mm^3 CdZnTe pixel. For each hit, the MGS simulator provided the signal induced at the cathode with a 10^{-9} s time step. All these hits were merged to generate single waveforms, as shown in figure 10. The timestamp was generated out of the waveform as the point where the induced voltage crossed the equivalent threshold to 10, 20 and 30 keV, and this value was compared with the timestamp value estimated by equation (10).

As is shown in figure 11, the accuracy of the prediction given by equation (10) depends on the energy threshold, but the actual error is very reasonable if it is taken into account that the absolute timestamp value can be as large as 10^{-7} s.

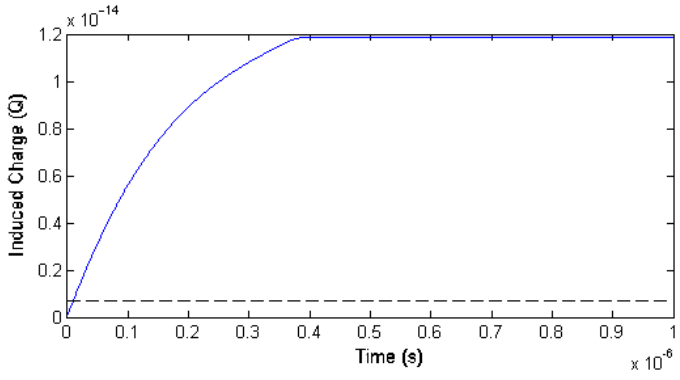

Figure 10. Cathode waveform for a 511 keV deposition.

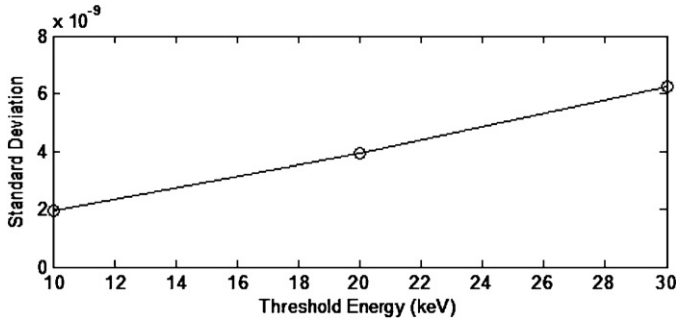

Figure 11. Standard deviation of the error in seconds between the model based and the MGS-computed cathode pulse shape.

3.2. Detector simulations

This section presents the results generated by GATE after the previously described models were included. Alike previous sections, a 5 × 5 pixel planar detector with a 2 × 2 × 5 mm^3 pixel size is simulated. With these detector dimensions, the values of τ_a and τ_c are estimated as 0.85 mm and 2.5 mm respectively. The timing setup takes into account the dependence on the point of interaction, where E_{trig} is set to 10 keV, and the electronic noise at the cathode, which is modelled as an additional 5 ns FWHM Gaussian degradation.

A line source filled with ^{57}Co placed at the centre of the field of view (FOV) is considered. ^{57}Co emits 14.4 keV (9.1%), 122 keV (85.6%) and 136.5 keV (10.7%) gamma photons. Additionally, material characteristic x-rays due to Cd (23.2 keV) and Te (27.5 keV) fluorescence are hardly visible except for the escape peaks that are observed as shoulders on the left of the 122 keV peak.

The simulated energy spectrum at the anode exhibits the characteristic tail expected on the low energy side of the spectrum, which is due to the rapid fall of the induced charge for interactions close to the anode, as shown in figure 12. Figure 13 presents the same data as seen by the cathode, where the weighting function can be considered close to linear. Both plots match very well with the experimental data reported by Li *et al* (2001). In addition, the demonstration of the simulated cathode energy versus the anode energy, shown in figure 14, matches the experimental biparametric data presented by d'Aillon *et al* (2005).

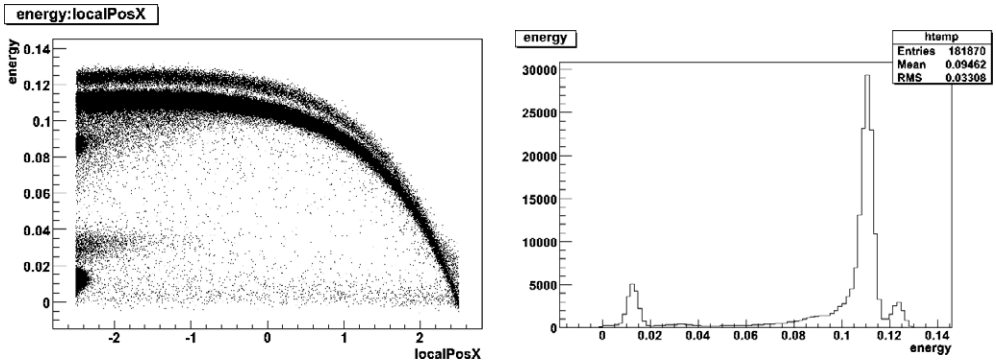

Figure 12. The simulated energy in MeV detected at the anode versus the depth of interaction in mm for a ^{57}Co source on the left and the resulting energy spectrum in MeV on the right.

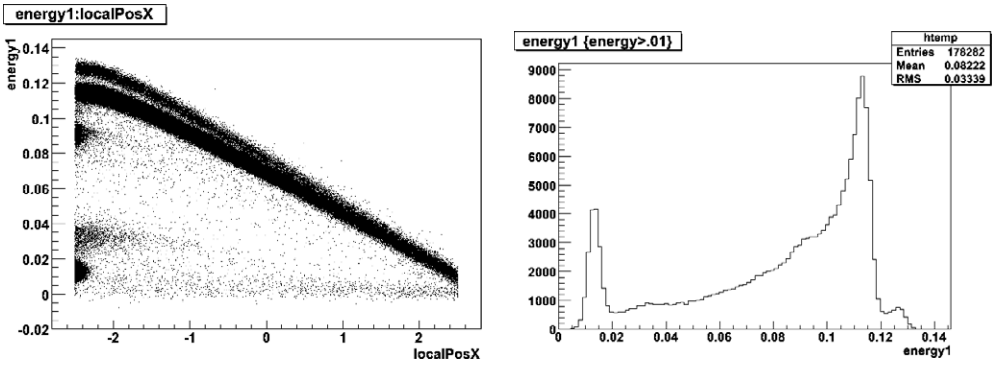

Figure 13. The simulated energy in MeV detected at the cathode versus the depth of interaction in mm for a ^{57}Co source on the left and the resulting energy spectrum in MeV on the right.

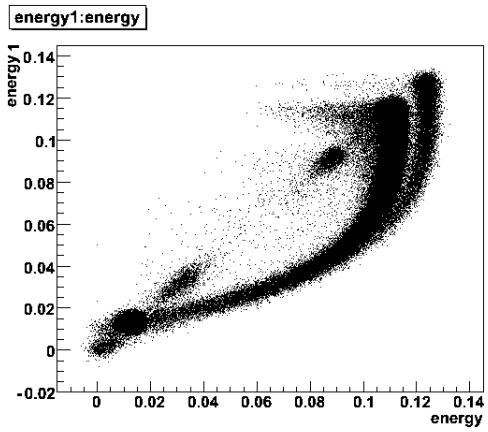

Figure 14. Cathode energy versus anode energy in MeV.

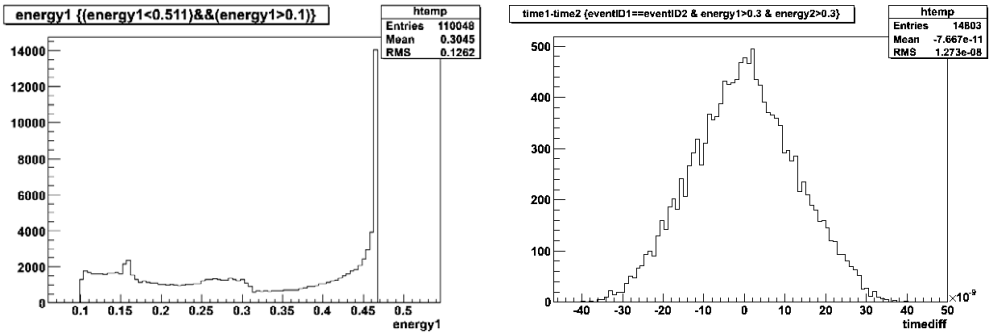

Figure 15. Energy spectra in MeV and timestamp difference distribution in seconds for 511 keV coincident events.

Simulations were also run for two 5 × 5 detectors with a pixel size of 10 × 10 × 5 mm^3, which were placed in coincident geometry, with a gamma source consisting of a 2 cm radius and 5 cm long plastic cylinder filled with ^{18}F at the centre of the FOV. Figure 15 shows the estimated energy spectra and timing resolution at 511 keV obtained as a result of these simulations. As a first approach, the timing resolution is estimated to be 30 ns FWHM; a value that accounts for the drift time between the interaction point and the collecting anode of the 5 mm thick CdZnTe slab and is consistent with published experimental results (Amrami *et al* 2000, Meng and He 2005, Okada *et al* 2002).

4. Discussion and conclusions

The GATE platform has been extensively validated against experimental data from numerous commercial scanners and has been consolidated as a design tool for the evaluation of new ideas and designs. However, existing systems focus primarily on scintillator-based detectors while semiconductor detectors, which are currently an interesting field of research for multimodality molecular imaging, are not modelled with the same level of detail.

A simplified model for pixellated semiconductor gamma-ray detectors has been integrated into the GATE environment in order to cover this gap. The implemented models take into account the geometry and the physics of the device charge collection and enable system simulations for accurate performance characterization of a multimodality imaging system at a computational cost which is at least three orders of magnitude lower than in the FEM model.

The provided simulations clearly show the dependence of the induction efficiency on the biasing conditions, material properties and depth of interaction. In practice, it can be argued that for a given isotope and for a selected energy threshold the detector will reject all interaction events that occurred within a material volume close to the anodes, unless biparametric techniques are employed in order to correct anode signals based on the energy read by the cathode. Based on these reasons, we may expect that previous works using GATE overestimate the sensitivity of a CdZnTe-based PET scanner as they neglect the importance of the small pixel effect on system performance.

These simulation models presented herein will be the cornerstone of future detailed simulations of an integrated multimodality system with the final aim of determining the optimum setup for a full-scale multimodal scanner based on pixellated CdZnTe detectors and assessing its performance potential. These simulations will aim at the best trade-off regarding

pixel size, thickness, operating bias and transport properties in order to guarantee the best possible energy, spatial and timing resolution for a wide range of energies, i.e. from tens of keVs of x-ray characteristics to the 511 keV of PET.

In addition, more accurate modelling of the induced cathode waveform is under consideration as the timing estimation presented here was obtained by neglecting electron recombination or trapping.

Acknowledgments

This project has been funded by the PDIMM project (CCG06-UPM/BIO-0502). We acknowledge Cayetano Santos from IRES for his initial support with the MGS internals and Bob Dirks from CEA Dapnia for providing the source code of his MGS version for CdZnTe.

References

Amrami R, Shani G, Hefetz Y, Levy M, Pansky A and Wainer N 2000 PET properties of pixellated CdZnTe detector *Engineering in Medicine and Biology Soc. 2000 Proc. 22nd Ann. Int. Conf. of the IEEE* pp 94–7

Barrett H H, Eskin J D and Barber H B 1995 Charge transport in arrays of semiconductor gamma-ray detectors *Phys. Rev. Lett.* **75** 156–9

Castoldi A, Gatti E and Rehak P 1996 Three-dimensional analytical solution of the Laplace equation suitable for semiconductor detector design *IEEE Trans. Nucl. Sci.* **43** 256–65

Cherry S R 2006 Multimodality in vivo imaging systems: twice the power or double the trouble? *Annu. Rev. Biomed. Eng.* **8** 35–62

d'Aillon E G, Gentet M C, Montemont G, Rustique J and Verger L 2005 Simulation and experimental results on monolithic CdZnTe gamma-ray detectors *IEEE Trans. Nucl. Sci.* **52** 3096–102

Darambara D G 2006 State-of-the-art radiation detectors for medical imaging: demands and trends *Nucl. Instrum. Methods Phys. Res.* A **569** 153–8

Dirks B P F, Limousin O, Ferrando P R and Chipaux R 2004 3D modeling of Cd(Zn)Te detectors for the Simbol-X space mission *Proc. SPIE High-Energy Detectors in Astronomy* pp 412–22

Funaki M, Ozaki T, Satoh K and Ohno R 1999 Growth and characterization of CdTe single crystals for radiation detectors *Nucl. Instrum. Methods Phys. Res.* A **436** 120–6

Glière A, Rosaz M and Verger L 2000 Simulation of CdZnTe gamma-ray spectrometer response *Nucl. Instrum. Methods Phys. Res.* A **442** 250–4

Habte F, Foudray A M K, Olcott P D and Levin C S 2007 Effects of system geometry and other physical factors on photon sensitivity of high-resolution positron emission tomography *Phys. Med. Biol.* **52** 3753–72

Hamel L-A and Paquet S 1996 Charge transport and signal generation in CdTe pixel detectors *Nucl. Instrum. Methods Phys. Res.* A **380** 238–40

He Z 2001 Review of the Shockley–Ramo theorem and its application in semiconductor gamma-ray detectors *Nucl. Instrum. Methods Phys. Res.* A **463** 250–67

Heanue J A, Brown J K and Hasegawa B H 1997 Two-dimensional modeling of Cd(Zn)Te strip detectors *IEEE Trans. Nucl. Sci.* **44** 701–7

Jan S, Comtat C, Strul D, Santin G and Trebossen R 2005 Monte Carlo Simulation for the ECAT EXACT HR+ system using GATE *IEEE Trans. Nucl. Sci.* **52** 627–33

Jan S, Comtat C, Trebossen R and Syrota A 2004 Monte Carlo simulation of the microPET focus for small animal *J. Nucl. Med.* **45** 420

Jan S *et al* 2004 GATE: a simulation toolkit for PET and SPECT *Phys. Med. Biol.* **49** 4543–61

Lamare F, Turzo A, Bizais Y and Visvikis D 2004 Simulation of the Allegro PET system using GATE *Proc. SPIE Medical Imaging Conf.* pp 890–7

Li W, He Z, Knoll G F, Wehe D K and Berry J E 2001 Experimental results from an Imarad 8×8 pixellated CZT detector *Nucl. Instrum. Methods Phys. Res.* A **458** 518–26

Mathy F, Gliere A, d'Aillon E G, Masse P, Picone M, Tabary J and Verger L 2004 A three-dimensional model of CdZnTe gamma-ray detector and its experimental validation *IEEE Trans. Nucl. Sci.* **51** 2419–26

Medina P, Santos C and Villaume D 2004 A simple method for the characterization of HPGe detectors *IEEE Instrumentation and Measurement Technology Conf. (Como, Italy)* pp 1828–32

Meng L J and He Z 2005 Exploring the limiting timing resolution for large volume CZT detectors with waveform analysis *Nucl. Instrum. Methods Phys. Res.* A **550** 435–45

Moseley M and Donnan G 2004 Multimodality imaging *Stroke* **35** 2632–4

Okada Y, Takahashi T, Sato G, Watanabe S, Nakazawa K, Mori K and Makishima K 2002 CdTe and CdZnTe detectors for timing measurements *IEEE Trans. Nucl. Sci.* **49** 1986

Picone M, Glière A and Massé P 2003 A three-dimensional model of CdZnTe gamma-ray spectrometer *Nucl. Instrum. Methods Phys. Res.* A **504** 313–6

Ramo S 1939 Currents induced by electron motion *Proc. Institute of Radio Engineers* pp 584–5

Schmidtlein C, Nehmeh S, Bidaut L, Erdi Y, Humm J, Amols H and Kirov A 2004 Validation of GATE Monte Carlo simulations for the GE advance PET scanner *J. Nucl. Med.* **45** 409–10

Schmidtlein C R, Kirov A S, Nehmeh S A, Erdi Y E, Humm J L and Amols H I 2006 Validation of GATE Monte Carlo simulations of the GE advance/discovery LS PET scanners *Med. Phys.* **33** 198–208

Seifert C E, Orrell J L, Coomes D E, LaMarche B L, Bliss M, Lynn K G, Jones K A and Campi G 2005 Performance of CdZnTe detectors grown by low-pressure Bridgman *IEEE Nucl. Sci. Symp. Conf. Rec.* **3** 1383–5

Szeles C 2004 Advances in the crystal growth and device fabrication technology of CdZnTe room temperature radiation detectors *IEEE Trans. Nucl. Sci.* **51** 1242–9

Szeles C and Eissler E E 1998 Current issues of high-pressure Bridgman growth of semi-insulating CdZnTe *Materials Research Society Symp.* pp 3–12

Visvikis D, Lefevre T, Kontaxakis G and Darambara D 2005 Monte Carlo based performance assessment of different animal PET scanner architectures using pixellated CZT detectors *ITBS2005-3rd Int. Conf. on Imaging Technologies in Biomedical Sciences (Milos, Greece)*

Wagenaar D *et al* 2007 Combined MRI-CZT SPECT Prototype Design Considerations at www.gammamedica.com/PDF/MRISPECT.pdf. (Gamma Medica-Ideas)